metals

Article

Hydrogen-Induced Delayed Fracture Susceptibility in Ti–Nb–V Microalloyed Press-Hardened Steel Compared to Ti-Microalloyed Reference

Renzo Valentini [1,*], Leonardo Bertini [2], Fabio D'Aiuto [3], Michele Maria Tedesco [4] and Hardy Mohrbacher [5,6]

[1] Department of Civil and Industrial Engineering, Pisa University, 56122 Pisa, Italy
[2] R&D Department, Letomec S.r.l., 56126 Pisa, Italy; l.bertini@letomec.com
[3] CBMM Europe BV, 1077 Amsterdam, The Netherlands; fabio.daiuto@cbmm.com
[4] Metals Department, Centro Ricerche Fiat S.C.p.A., 10135 Turin, Italy; michelemaria.tedesco@crf.it
[5] NiobelCon BV, 2970 Schilde, Belgium; hm@niobelcon.net
[6] Department of Materials Engineering (MTM), KU Leuven, 3001 Leuven, Belgium
* Correspondence: renzo.valentini@unipi.it

Abstract

In alignment with the European Union's 2050 carbon-neutrality targets, the automotive industry is intensifying efforts to adopt lightweight materials that ensure structural integrity without compromising safety. Press-hardened steels (PHS), offering a combination of ultra-high strength and formability, are at the forefront of these developments. Standard PHS grades rely on Ti–B microalloying; however, further alloying with Nb and V has been proposed to enhance hydrogen embrittlement resistance via microstructural refinement and hydrogen trapping. This study investigates hydrogen transport and mechanical degradation in a Ti–Nb–V microalloyed PHS compared to a conventional Ti-only 22MnB5 grade. Electrochemical permeation, thermal desorption, and mechanical testing were employed to characterize hydrogen diffusivity, solubility, and trapping mechanisms. The Ti–Nb–V variant demonstrated lower hydrogen diffusivity, higher solubility, and improved resistance to delayed fracture, attributable to the presence of fine NbTiV precipitates.

Keywords: press hardening steel; microalloying; hydrogen embrittlement; carbide precipitates; diffusible hydrogen; delayed fracture; grain refinement

Check for updates

Academic Editor: Gang Niu

Received: 5 December 2025
Revised: 14 January 2026
Accepted: 19 January 2026
Published: 28 January 2026

Copyright: © 2026 by the authors. Licensee MDPI, Basel, Switzerland. This article is an open access article distributed under the terms and conditions of the Creative Commons Attribution (CC BY) license.

1. Introduction

Reducing vehicle weight is a key strategy for lowering fuel consumption and CO_2 emissions in the automotive sector. In this context, the use of advanced materials capable of meeting increasingly stringent safety and durability requirements while enabling lightweight design has become essential. Advanced High Strength Steels (AHSS), and, in particular, press-hardened steels (PHS), play a central role thanks to their exceptional strength-to-weight ratio and industrial maturity. A comprehensive overview of hot-stamping technology and its application in the vehicle industry is given in [1].

PHS grades undergo hot forming in austenitic condition followed by rapid in-die quenching, resulting in a fully martensitic microstructure. These steels are widely employed in structural automotive components such as A- and B-pillars and crash-relevant reinforcements. Considering these applications, reliable performance of such steels regarding resistance against crack initiation and propagation is a key requirement. Lacking such resistance can result in unexpected component disintegration under dynamic or even

static load conditions with catastrophic consequences for vehicle safety. Related material characteristics allowing us to quantify the performance and to define industrial quality criteria are Charpy toughness [2], critical bending angle (acc. to VDA238-100) [3,4], fracture strain [5,6] and the essential work of fracture [7].

Hydrogen-induced delayed fracture (HIDF) sensitivity represents another critical reliability concern for press-hardened steels that exponentially increases with the strength level. This damage phenomenon arises from the presence of hydrogen in combination with applied or residual stresses and is characterized by time-dependent failure occurring after hydrogen ingress. Typical propagation modes of hydrogen-related cracks in martensitic steel are of quasi-cleavage and intergranular nature [8]. Several mechanisms have been proposed to explain the progress of hydrogen-assisted fracture in steels, including hydrogen-enhanced decohesion (HEDE), hydrogen-enhanced localized plasticity (HELP), and hydrogen-enhanced strain-induced vacancy (HESIV) formation [9–12]. Accordingly, the fracture surface typically has a brittle appearance yet is not excluding elements of ductile origin.

From a mitigation standpoint, several complementary strategies have been proposed to reduce hydrogen-assisted delayed fracture in press-hardened martensitic steels. Microstructural refinement, particularly through control of prior austenite grain size and martensitic substructure, has been shown to influence hydrogen transport and embrittlement susceptibility in ultra-high strength PHS grades [13]. The introduction of hydrogen traps with different binding strengths can effectively reduce the amount of diffusible hydrogen available for embrittlement [14,15]. However, reversible traps, such as dislocations and grain or lath boundaries, can only temporarily immobilize hydrogen, whereas deep or irreversible traps associated with nanoscale carbide precipitates (e.g., NbC or complex Nb–Ti–V carbides) can more effectively reduce the amount of diffusible hydrogen available for embrittlement [15,16]. Deep trapping of hydrogen can completely neutralize a certain amount of hydrogen. However, this trapping capacity is limited and will saturate in a continuous hydrogen supply scenario.

Related to PHS, all three microalloying elements (Ti, Nb, V) principally have the capability of forming particles capable of hydrogen trapping. Recent works succeeded in identifying the presence of hydrogen atoms at the particle–matrix interface of microalloy carbides [17–19]. For carbides at the same carbon composition, the magnitude of the interaction energy derived from TDS measurements, which characterizes its hydrogen-trapping ability, has been ranked in the following order: NbCx > TiCx > VCx (x < 1 denotes a sub-stoichiometric carbide composition) [16,20]. While this ranking applies only to (semi-)coherent particles, it was stated that incoherent NbC and VC particles contrary to TiC were unable to trap hydrogen.

PHS grades rely on a simple carbon–manganese base alloy concept which is standardly microalloyed with boron and titanium. Thereby, boron provides sufficient hardenability during die quenching while titanium is added to protect boron from binding with residual nitrogen. Typically, the titanium addition level is over-stoichiometric to nitrogen so that excess titanium can form TiC particles with carbon. In various attempts to optimize PHS performance, alloy design variations employing additional microalloying—most notably with niobium and molybdenum, and in some developments with vanadium—have been explored [13]. The primary intention is to refine the microstructure and to delay damage initiation and propagation at strength levels exceeding 1500 MPa. Nano-sized microalloy carbide precipitates are known to significantly influence performance by refining the microstructure and improving microstructural uniformity [13,21–25]. Furthermore, resistance to delayed cracking could be enhanced by providing hydrogen trapping as outlined before. In addition, coatings and process-related factors—including coating integrity, press-

hardening thermal cycles, and post-forming heat treatments—play an important role in governing hydrogen entry, transport, and desorption, and must, therefore, be considered when assessing the hydrogen embrittlement risk in coated PHS components [26].

In this study, the susceptibility to hydrogen-induced delayed fracture of a commercially produced NbV microalloyed press-hardened steel is investigated and compared with that of a conventional Ti-microalloyed 22MnB5 reference steel. Both materials are classified as PHS 1500 grades and were processed under identical press-hardening conditions. In a previous study, the microstructure of these steels was investigated in great detail at the different processing steps [27]. The results of this study indicated that single titanium microalloying does not provide a stable nanoprecipitate population obstructing grain coarsening during the austenitizing treatment before hot stamping. This was reasoned by partial dissolution and Ostwald ripening of titanium carbide particles in the intercritical temperature range. However, ultrafine particles consisting of a mixed Ti–Nb–V carbide and with a homogeneous spatial distribution were present in the NbV microalloyed PHS after press hardening and baking in agreement with [28]. These particles were found to be incoherent with the martensitic matrix as expected. The ultrafine particle population was shown to allow austenite grain-size control to result in generally finer martensitic microstructure especially also after overheating conditions.

The present study systematically investigates the hydrogen transport properties, trapping energetics, and mechanical degradation under hydrogen exposure using electrochemical permeation, thermal desorption analysis (TDS), and slow strain-rate testing. In addition, an accelerated corrosion test in a salt spray environment was performed to assess potential hydrogen uptake during service-related exposure. It will be analyzed whether the microstructural refinement enhances resistance to hydrogen-induced delayed fracture in the press-hardened steel as was already found in TiNb microalloyed PHS. Moreover, TDS analysis allows verifying whether the ultrafine-sized and incoherent Ti–Nb–V carbides are capable of hydrogen trapping.

2. Materials and Methods

Two 22MnB5 steels, supplied by Centro Ricerche Fiat S.C.p.A., Turin, Italy, with different microalloying strategies—one using the standard B–Ti concept and the other using a multiple microalloy concept with B–Ti–Nb–V (Table 1)—were evaluated in this study. Both steels, with a thickness of 1.2 mm, originated from industrial production and were AlSi-coated (AS40). Sheets were cut from the coils and heat treated in a laboratory furnace. A standard thermal cycle, representative of automotive hot-stamping processes, was applied by austenitizing at 915 °C for 8 min. Part of the samples also underwent a paint-baking heat treatment, simulating industrial conditions, by holding the as-quenched steel at 170 °C for 20 min.

Table 1. Chemical composition (%) of 22MnB5 press hardening steels, Fe the balance.

	C	Si	Mn	Cr	N	Ti	Nb	V	B
Standard PHS	0.24	0.25	1.31	0.18	0.003	0.03	-	-	0.002
NbV PHS	0.20	0.28	1.21	0.17	0.003	0.03	0.04	0.04	0.002

In both steels, the Ti/N ratio is approximately 10:1, significantly exceeding the stoichiometric ratio of 3.4:1. This promotes the primary precipitation of coarse TiN particles. Microstructural characterization confirmed the presence of such coarse TiN precipitates [8]. However, a significant amount of Ti (estimated at ~0.02 wt%) remains available for the

precipitation of fine TiC particles. Most Nb and V form carbides, which were identified as mixed Ti–Nb–V carbides, as detailed in [27].

The following sections describe the experimental methodologies used in this study. These methods enabled the evaluation of differences in hydrogen diffusivity, hydrogen-trapping activation energy, and mechanical performance between the two alloy designs. Samples for mechanical testing were laser cut before heat treatment using geometries defined in the relevant standards. An additional series of hydrogen measurements was carried out to evaluate hydrogen content before and after heat treatment.

2.1. Hydrogen Diffusivity

Electrochemical permeation tests were performed to determine the effective hydrogen diffusion coefficient, following the procedure outlined in [29] using HELIOS 2 equipment [15]. After mechanical removing of the coating by grinding with SiC400 paper, the surface had been ground with a SiC600 and degreased in acetone. The surface area was circular with a diameter of 0.02 m. The test solution was a mixture of 30 g/L of sodium chloride (NaCl) and ammonium thiocyanate (NH_4SCN) 0.3% added as a hydrogen promoter. A cathodic charging current of -10 A m^{-2} was applied in galvanostatic mode. Tests were conducted at various temperatures after standard heat treatment, both with and without coating on the exit (detection) side, for both the Ti-only and Ti–Nb–V steels. The effective hydrogen diffusion coefficient was calculated using the 63% method, defined by Equation (1):

$$D = \frac{L^2}{6\, t_{63}} \tag{1}$$

where

- D is the effective hydrogen diffusion coefficient,
- L is the specimen thickness,
- t_{63} is the time required for the hydrogen flux at the exit surface to reach 63% of the steady-state value.

2.2. Activation Energies of Hydrogen-Trapping Sites

The diffusion coefficients measured at different temperatures were used to estimate the binding energies of low-energy hydrogen traps. A linear regression fitting on logarithmic coordinates was applied, based on the Arrhenius-type Equation (2) [30]:

$$D_{app} = A\, e^{\left(-\frac{B}{RT}\right)} \tag{2}$$

where

- A is a pre-exponential factor,
- B is the apparent activation energy (in J/mol),
- R is the universal gas constant,
- T is the absolute temperature.

The parameters A and B can be expressed as

$$A = D_0 \frac{N_l}{N_r} \tag{3}$$

$$B = E_b + E_l \tag{4}$$

where

- D_0 is the pre-exponential diffusion coefficient,
- N_l is the density of lattice sites per unit volume,

- N_r is the density of trap sites per unit volume,
- E_b is the binding energy of traps,
- E_l is the activation energy for hydrogen movement between lattice sites.

The apparent activation energy was estimated from an Arrhenius-type analysis of the effective hydrogen diffusion coefficient measured at different temperatures. The logarithm of the apparent diffusion coefficient was plotted as a function of the inverse absolute temperature, and the activation energy was obtained from the slope of a linear regression according to Equation (2). The regression was performed over the investigated temperature range assuming a single dominant trapping contribution within this interval. The uncertainty associated with the activation energy mainly arises from experimental scatter in diffusion time determination and specimen thickness measurement; these sources of error are reflected in the regression uncertainty.

Alternatively, Temperature Programmed Desorption (TPD) tests were used to study the physical desorption behavior as a function of temperature. Sheet specimens (12×30 mm^2) were hydrogen-charged during heat treatment in a laboratory furnace under controlled humidity conditions. These were subsequently heated from room temperature to 500 °C at rates ranging from 1 to 7 °C/min. TPD curves were analyzed using Gaussian peak deconvolution to identify trap energies [26].

2.3. Mechanical Behavior

Slow Strain Rate Tests (SSRTs) were conducted according to [31] to correlate hydrogen absorption with mechanical degradation, specifically reductions in strength and elongation at break. The test specimen geometry followed the guidelines in [32] and is shown in Figure 1.

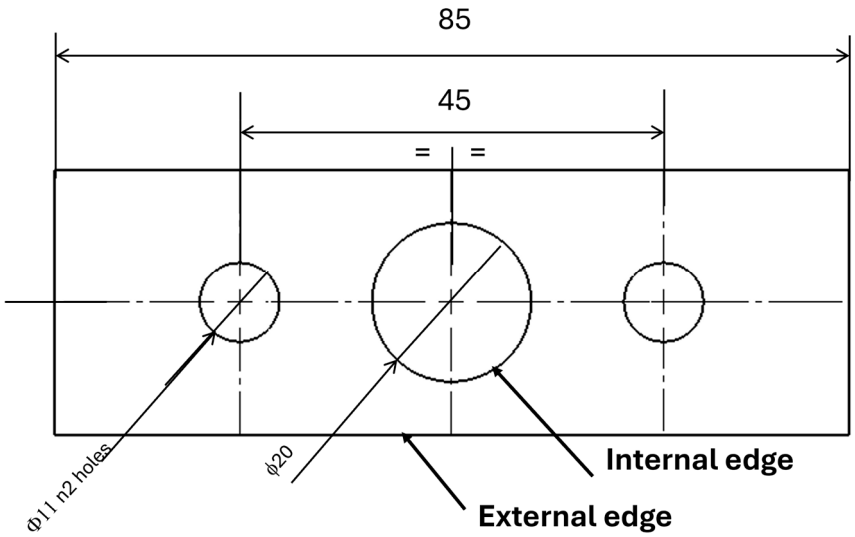


Figure 1. Edges identification for fractographic analysis.

Tests were conducted on hydrogen-precharged specimens. Some samples were charged via hot furnace charging with varied furnace dew points from −15 to 20 °C, according to the literature data [33], while others underwent standard heat treatment (915 °C for 8 min) followed by cathodic charging. For cathodic hydrogen charging, the steel specimens acted as the working electrode in an aqueous solution containing 30 g·L^{-1} sodium chloride (NaCl), with ammonium thiocyanate (NH_4SCN) added as a hydrogen recombination inhibitor in the range of 2–6 g·L^{-1}. Hydrogen charging was performed under galvanostatic conditions at room temperature, using applied current densities between −2.5 and −25 A·m^{-2}. Charging was carried out for 16 h, a duration selected to

ensure a homogeneous hydrogen distribution across the specimen thickness, as estimated from the hydrogen diffusion coefficient. Nitrogen bubbling was applied during charging to minimize oxygen content in the electrolyte. A combination of charging current density and inhibitor concentration was used to obtain a wide range of diffusible hydrogen contents in the investigated steels. Hydrogen charging was performed at room temperature under nitrogen bubbling. The parameters reported above represent nominal charging conditions and operational ranges used to generate controlled levels of diffusible hydrogen; minor specimen-to-specimen variations inherent to electrochemical charging were not individually recorded, as the study focused on comparative trends rather than absolute charging efficiency.

All samples underwent a paint-baking simulation (170 °C for 20 min) prior to testing. This treatment is known to reduce the diffusible hydrogen content, as the AlSi coating acts as a diffusion barrier up to approximately 75 °C; at higher temperatures, hydrogen effusion begins [33].

The expected reduction in diffusible hydrogen content associated with the paint-baking treatment was explicitly considered when defining the hydrogen charging conditions for mechanical testing. A constant strain rate of 10^{-3} mm/s was applied. For each hydrogen charging condition, at least two specimens were tested to verify the reproducibility of the observed mechanical response. After testing, the diffusible hydrogen content was measured via hot gas extraction at 265 °C—a temperature selected to minimize the influence of coating decomposition, as suggested in [33].

The experimental data were fitted using a regression model based on Equation (5):

$$A = m_1 - m_2 atan\left(\frac{C_H - m_3}{m_4}\right) \quad (5)$$

where

- A is a property related to mechanical performance (e.g., elongation or strength),
- C_H is the diffusible hydrogen content,
- m_1–m_4 are fitting parameters.

3. Results

3.1. Hydrogen Diffusivity

Before heat treatment, the hydrogen diffusion coefficients of 22MnB5 and NbV steels are nearly identical and lower than historical reference values—likely due to higher titanium content and finer prior austenite grain size. After heat treatment, however, the diffusion coefficient of the NbV steel is significantly lower, indicating the influence of niobium addition.

Table 2 summarizes the hydrogen diffusion coefficients at 30 °C after heat treatment (915 °C × 8 min + 170 °C × 20 min), comparing values for bare steel and steel with AS40 coating on the exit side to assess the coating's barrier effect.

Table 2. Effective hydrogen diffusion coefficient at 30 °C with and without AS coating.

Material	H Diffusion Coefficient (m^2/s)	
	Without Coating	AS40 on Exit Side
22MnB5	8.73×10^{-11}	6.28×10^{-11}
NbV	7.16×10^{-11}	3.83×10^{-11}

3.2. Activation Energies of Hydrogen-Trapping Sites

Electrochemical permeation tests were repeated at various temperatures on heat-treated (quenched + paint-baked) steels. The AS40 coating was removed prior to testing. Activation energies for low-energy, reversible hydrogen traps were determined following the method described in Section 2.2. Results are illustrated in Figure 2. Error bars on the *x*-axis reflect temperature variation; those on the *y*-axis represent instrument error during thickness measurement. The estimated activation energies were 26.5 kJ/mol for 22MnB5 and 25.4 kJ/mol for the NbV variant.

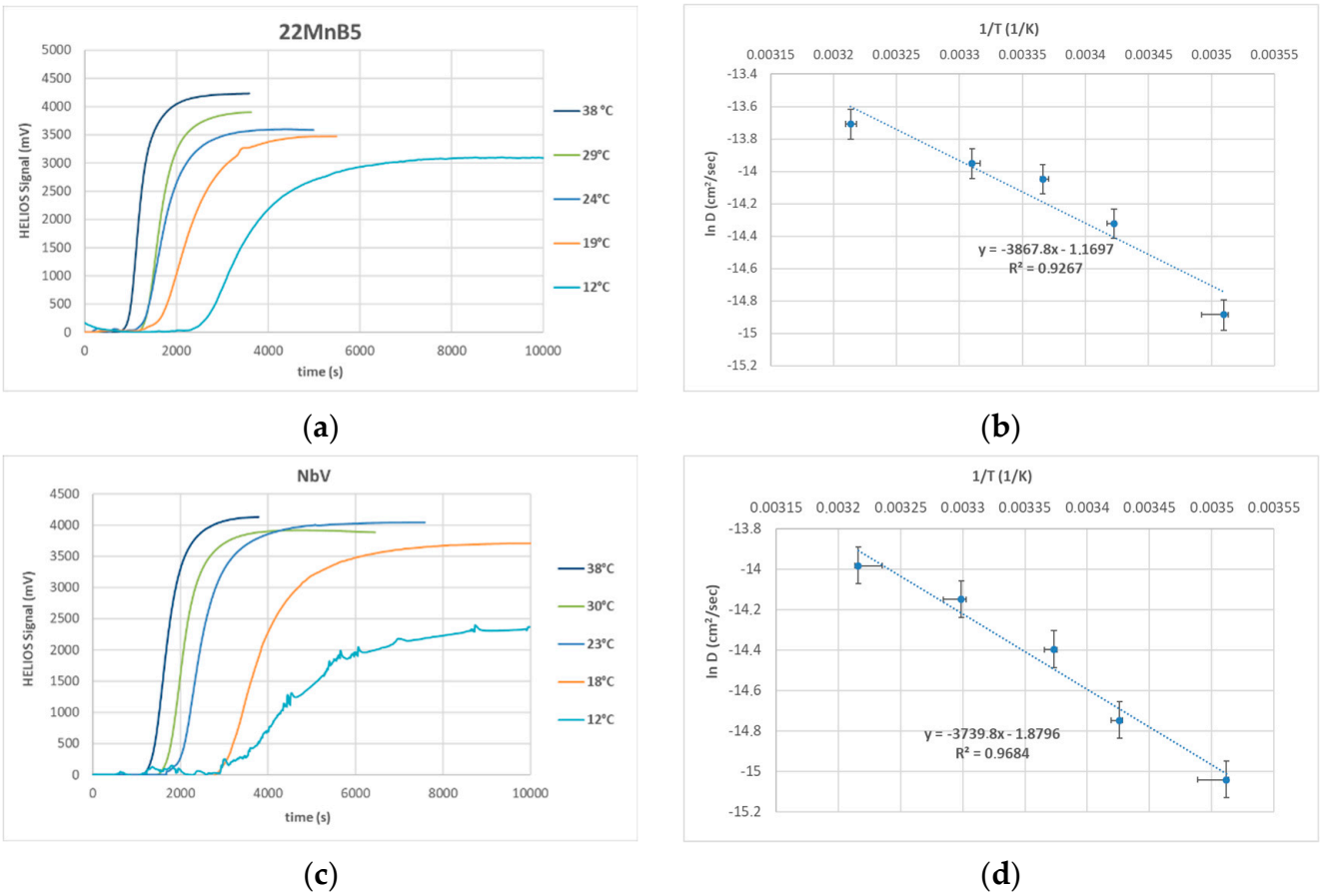
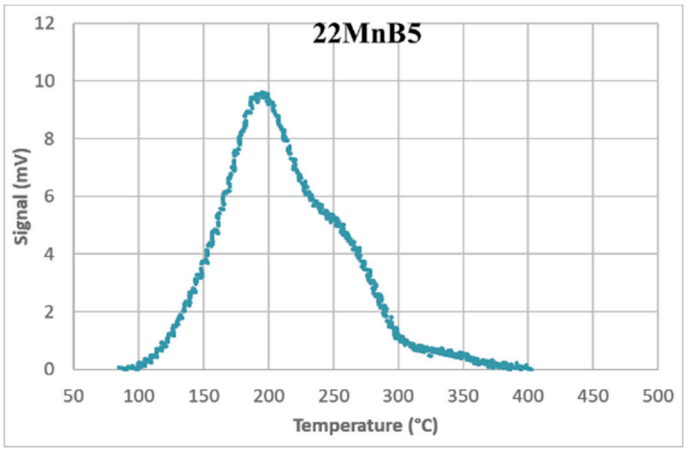
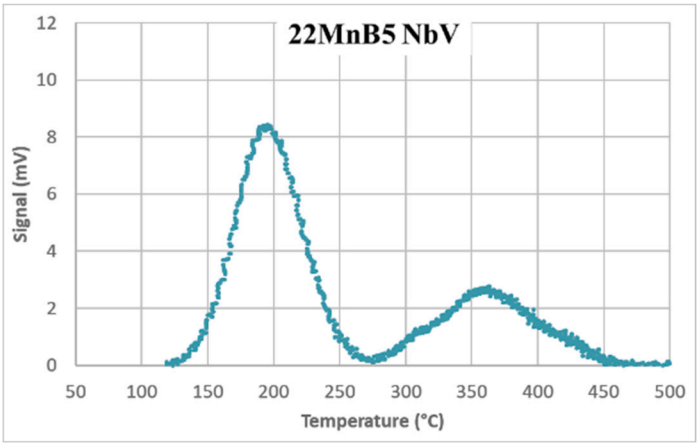


Figure 2. Permeation curves and regression of 22MnB5 (**a**,**b**) and NbV variant (**c**,**d**).

Temperature Programmed Desorption (TPD) was then used to characterize hydrogen traps. After hot furnace hydrogen charging, the AS40 coating was removed. Specimens were subjected to heating rates (Φ) from 1 to 7 °C/min. The hydrogen desorption signal was analyzed to determine peak temperatures via Gaussian deconvolution (Figure 3). The apparent shoulder visible in the desorption curve shown in Figure 3 a does not correspond to a distinct hydrogen-trapping site. Reliable identification of individual trapping contributions requires regression over multiple heating rates, as performed in Figure 2, where a second high-energy trap is clearly identified only for the NbV steel. The desorption curve reported in Figure 4 is shown as a representative example obtained at a heating rate of 10 K·min^{-1}, whereas the activation energies were extracted from regression analysis performed over multiple heating rates in the range of 1–7 K·min^{-1}, as summarized in Figure 4.



(**a**)



(**b**)

Figure 3. Examples of temperature programmed desorption curves for (**a**) 22MnB5 and (**b**) NbV variant, with heating rate equal to 10 K/min.

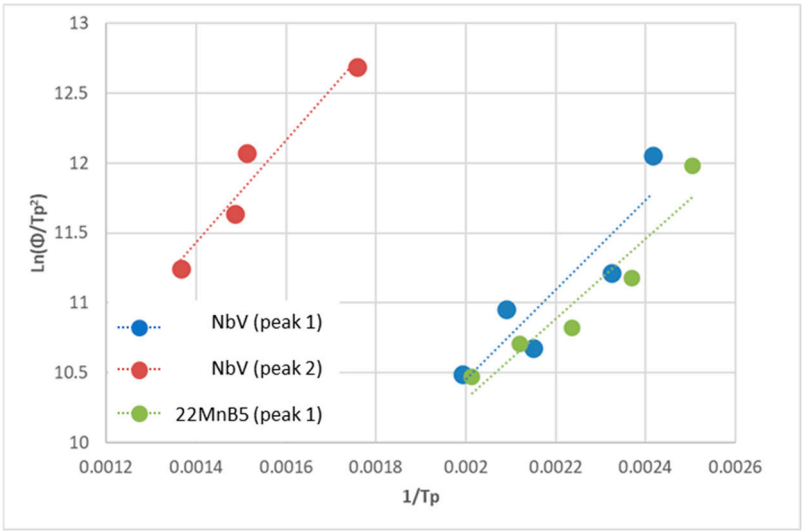


Figure 4. TPD regression lines for 22MnB5 and NbV variant.

Table 3 lists the activation energies calculated from the regression analysis. The first peak is observed in both steels and corresponds to trapping at grain boundaries and dislocations. A second, higher-energy peak is visible only in the NbV PHS and is attributed to hydrogen-trapping at the microalloy precipitates.

Table 3. Activation energies for hydrogen traps.

Material	Activation Energy (kJ/mol)	
	Peak 1	Peak 2
22MnB5	23.8	-
NbV	26.5	30.4

3.3. Mechanical Behavior

Figure 5 displays the ultimate tensile strength (a) and crosshead displacement at break (b) versus diffusible hydrogen content. Due to sample geometry (SEP 1970:2011 [32]), an extensometer could not be used. Two performance plateaus are evident. Up to ~1.0 ppmw hydrogen, both steels retain full ductility and strength. Above ~2.5 ppmw, full embrittlement occurs. The Ti–Nb–V steel exhibits a more gradual transition and a higher critical hydrogen content, as fitted using Equation (5) (see Section 2.3). The critical hydrogen content (corresponding to a 30% drop in mechanical performance) was

- 22MnB5: 1.7 ppmw
- NbV: 2.2 ppmw

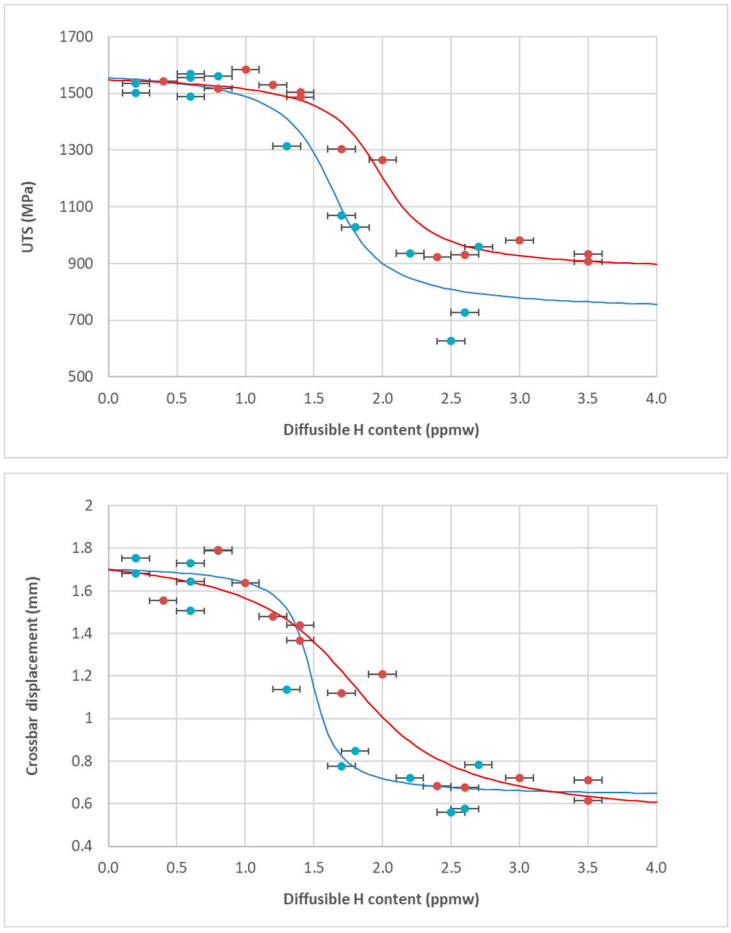
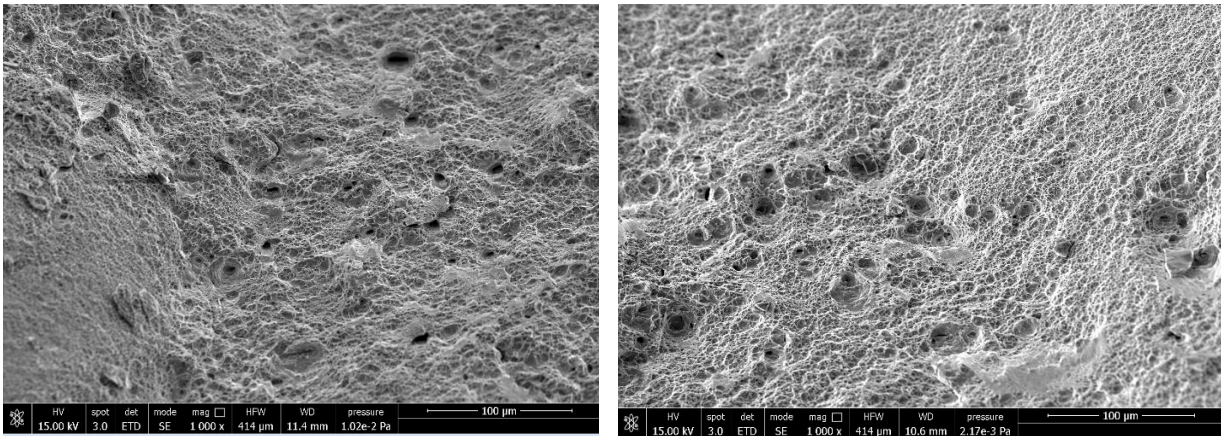


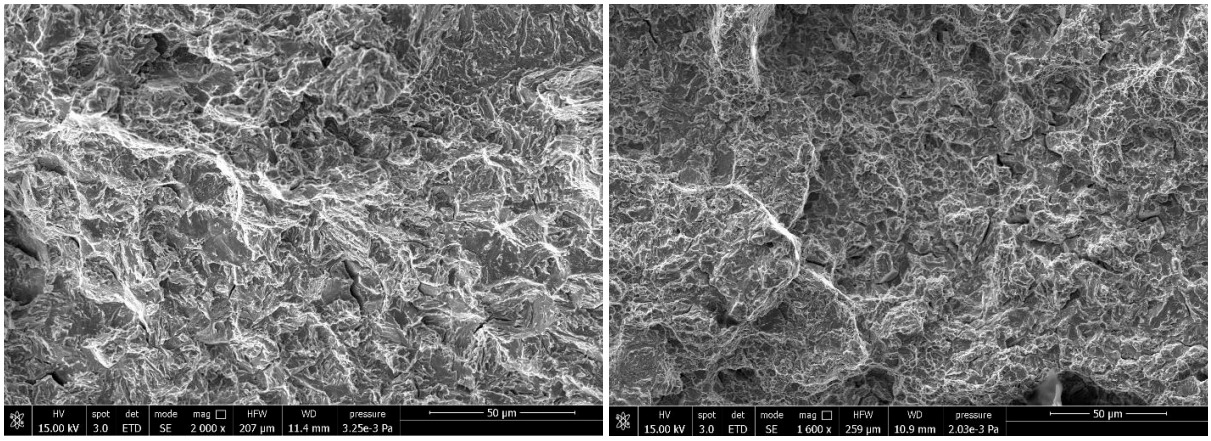
Figure 5. Regression curve and experimental data of (**a**) UTS vs. C_H, and (**b**) crossbar displacement vs. C_H resulting from SSRT on 22MnB5 in blue and NbV in red.

Fractography using scanning electron microscopy was performed on fracture surfaces at various hydrogen levels. For low hydrogen content, both steels show predominantly ductile (dimpled) fractures (Figure 6), while high hydrogen content results in quasi-cleavage and intergranular fracture (Figure 7).



(**a**) (**b**)

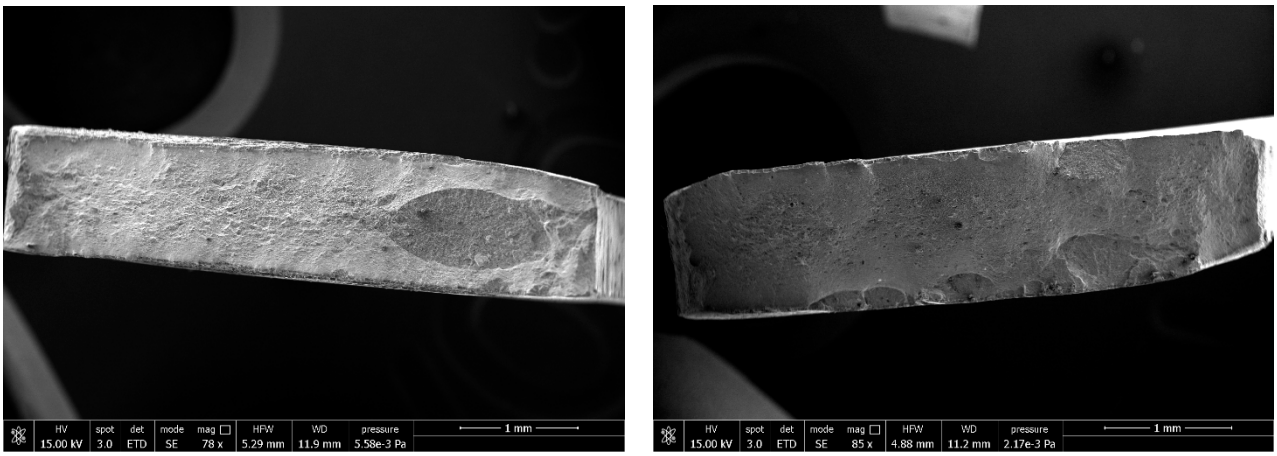
Figure 6. Fracture surfaces of samples with low hydrogen level, (**a**) 22MnB5 external edge, and (**b**) NbV internal edge.



(**a**) (**b**)

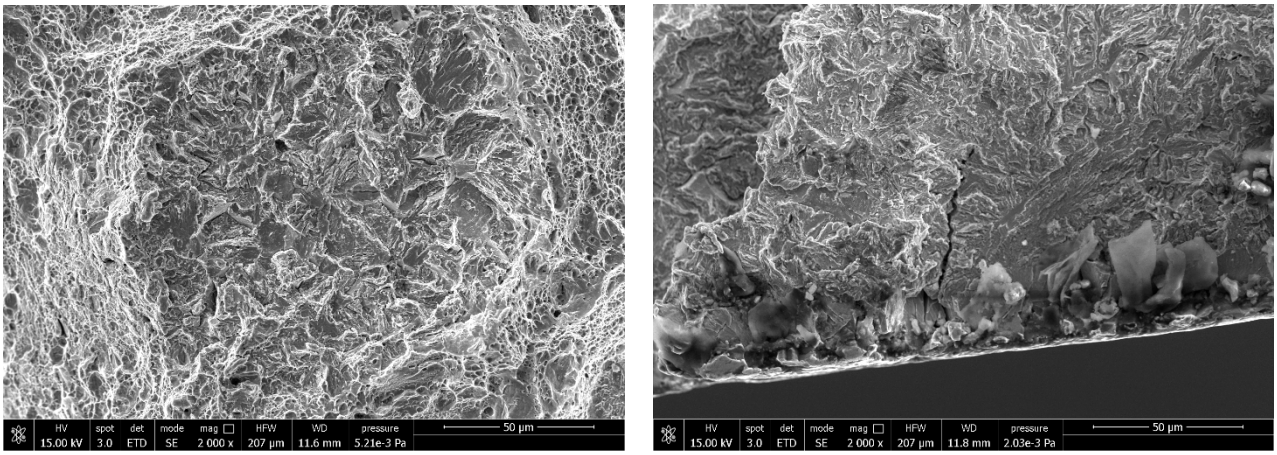
Figure 7. Fracture surfaces of samples with high hydrogen level, (**a**) 22MnB5 external edge, and (**b**) NbV at the core.

At ~1.7 ppmw hydrogen (transition range), mixed fractures were observed in both steels (Figure 8). In the TiNbV steel, brittle regions were localized near the AlSi interdiffusion layer, with the midsection remaining ductile.



(**a**) (**b**)

Figure 8. *Cont.*



(**c**) (**d**)

Figure 8. SEM images of fracture surfaces in sample containing 1.7 ppmw: (**a**,**c**) 22MnB5 sample and internal edge with brittle area exposing quasi-cleavage type of fracture surrounded by areas of ductile behavior; (**b**,**d**) NbV sample edge exposing smaller areas of quasi-cleavage fracture close to the interdiffusion layer of the AlSi coating.

4. Discussion

Hydrogen has a detrimental effect on both tensile strength and ductility. This is particularly important for automotive applications, where energy absorption (UTS × displacement) is a critical performance criterion. Figure 9 shows that post-embrittlement performance drops to ~22% of the original energy absorption. The transition region is linear for both steels with nearly the same slope. However, the NbV variant tolerates ~0.5 ppmw more hydrogen. This suggests that this amount of hydrogen has been trapped to a degree sufficient to immobilize it.

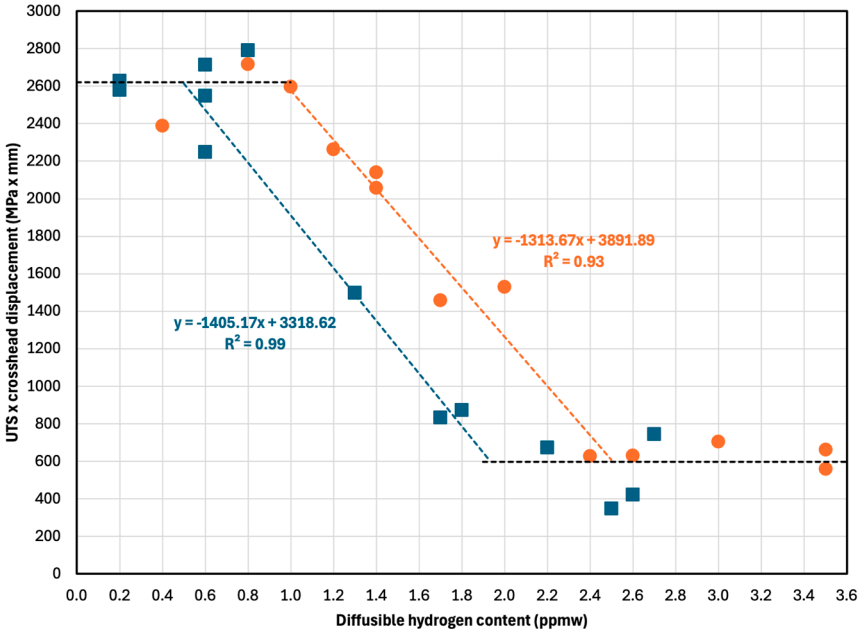


Figure 9. Dependence of energy-absorption criterion (defined as UTS x crosshead displacement) on the diffusible hydrogen content; ductile and brittle plateaus with equal performance of both steels; transition region with advantageous performance of the NbV steel tolerating approx. 0.5 ppmw more diffusible hydrogen.

Strain rate effects, as shown by Momotani et al. [34], suggest hydrogen accumulation at prior austenite grain boundaries (PAGBs) during low strain-rate testing. With lower hydrogen diffusivity (as is the case in the NbV PHS), embrittlement of PAGBs is delayed. Under constant load (delayed fracture) conditions, grain size becomes decisive [13]. Niobium microalloying, as previously shown [12,23,24], as well as NbV microalloying [21,27] promote finer grain size by pinning effects of nano-carbide precipitates.

In the ductile range, hydrogen enhances dislocation mobility (HELP mechanism), suppressing work hardening. At higher concentrations, brittle fracture dominates due to HELP and HEDE mechanisms acting locally in areas of stress concentration (e.g., at the circular notch in SEP samples). PAGBs, saturated with hydrogen, become preferential fracture paths. Grain refinement dilutes hydrogen across a larger total grain boundary surface, delaying embrittlement [13,35].

The nearly constant 0.5 ppmw offset between the investigated steels effectively implies an additional hydrogen-trapping potential in the NbV steel, attributed to nano-sized carbides. These particles have a spherical morphology, 8 nm average diameter, mixed Ti–Nb–V composition, and a number density of ~3000–3500/μm^3. Figure 10 represents transmission electron micrographs of such particles. For a detailed microstructural characterization, the reader is referred to a prior publication on these steels [27]. Assuming the number density of hydrogen atoms per unit area being 1–5 atoms nm^{-2} according to prior investigations by Ohnuma et al. [19], the particle population in the current NbV steel could theoretically trap ~0.6 ppmw hydrogen, which is in good agreement with the measured offset of 0.5 ppmw relative to the standard PHS.

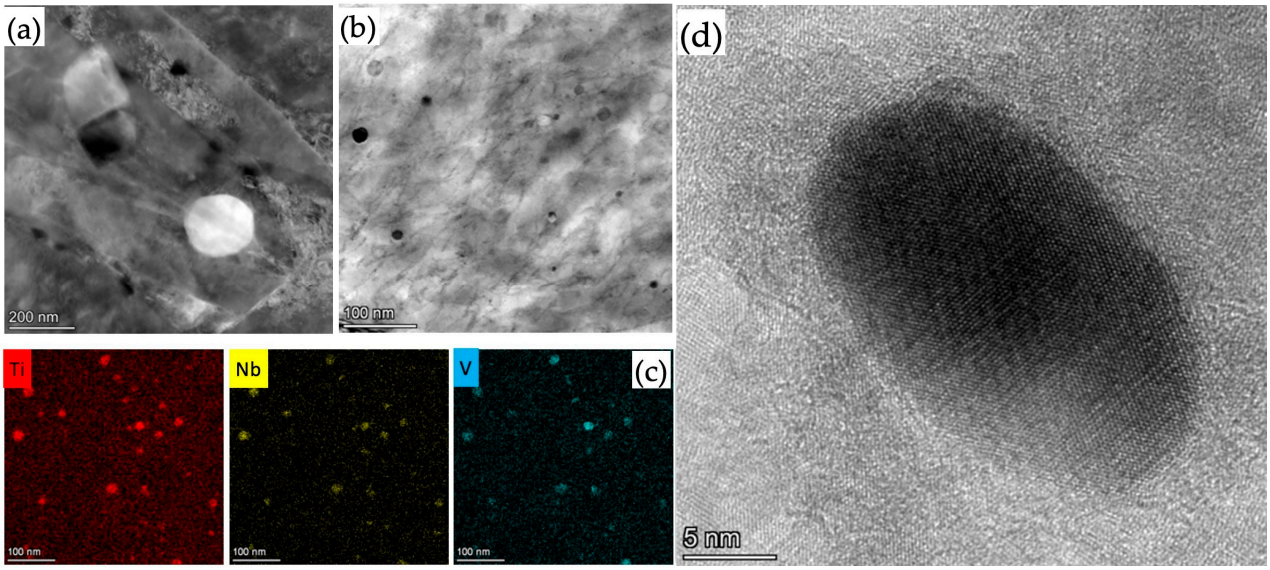


Figure 10. Representative transmission electron micrographs in through transmission bright field mode (**a**,**b**); energy dispersive analysis of microalloy presence in the particles (**c**); high resolution image of an incoherent Nb−Ti−V carbide precipitate (**d**).

The observed trapping energy (30.5 kJ/mol) represented by peak 2 in the NbV steel (Figure 2b) is in the range of values reported in the literature for precipitates formed by microalloy carbides [36–38]. The sequence of processing conditions in press hardening are expected to predominantly produce precipitates with an incoherent particle–matrix interface. The original formation of nano-sized microalloy carbides proceeds during (a) coiling, (b) recrystallization annealing after cold rolling and (c) up-heating to austenite temperature in the hot-stamping cycle. The nucleation of the particles always occurs in the ferrite phase with a Baker–Nutting orientation relationship leading to a disk-shaped

particle morphology. However, no favorable nucleation scenario exists for austenite in the absence of plastic deformation. Preexisting disk-shaped particles that had a (semi-)coherent interface in ferrite lose coherency upon phase transformation to austenite accompanied by a change to spheroidal or ellipsoidal morphology [20,39]. The transformation into martensite upon quenching cannot reinstall coherency between the newly formed bcc matrix and the preexisting particle.

The interface between an incoherent particle and the matrix represents a phase boundary without featuring long-range hydrogen attraction towards the carbide interface due to the absence of elastic interactions related to interfacial strain fields. According to a theoretical analysis by Zhang et al. [40], hydrogen atoms are more likely to be attracted to the broad sides of disk-shaped (semi-)coherent carbide precipitates while there is no active hydrogen attraction to incoherent precipitates. Nevertheless, diffusing hydrogen atoms can coincidentally encounter the phase boundary of incoherent particles. The probability for such encounters increases with increasing particle volume fraction and decreasing mean interparticle spacing. Zhang et al. [41] argued that hydrogen trapping at the phase boundary between a MC particle and the ferrite matrix relies on mechanical and chemical contributions. The latter, involving a charge transfer of the local atomic environment at the phase boundary and hydrogen, might even be the dominant effect. The binding energy depends on hydrogen's occupational site at the phase boundary as well as the transition metal forming the carbide. Hydrogen-binding energies at various interstitial sites at the MC–matrix phase boundary range between 0.1 and 1.2 eV (~10–115 kJ/mol). Carbon vacancies represent the deepest traps (>1 eV) yet have a high energy barrier that cannot be overcome at ambient temperature. However, the energy barrier can be reduced if the carbide particle features percolating networks of C vacancies as can be expected in sub-stoichiometric carbides. Consequently, it is impossible to specify a generally valid single value for hydrogen binding energy at a MC–matrix phase boundary and especially not for the present mixed Ti–Nb–V carbide species. However, the measured value of approximately 0.3 eV (~29 kJ/mol) is quite well matched with values calculated by DFT for binary TiC and NbC, while VC shows lower binding energies [41].

The major share of the added vanadium remains solute after press hardening and is, thus, available for precipitating VC particles during post-processing like welding or high-temperature tempering. Such ad hoc formed carbides necessarily establish a (semi-)coherent interface with the tempered martensite matrix according to a Baker–Nutting orientation relationship, as mentioned before. The particles provide additional hydrogen-trapping sites and partially compensate for the softening of the matrix [42]. However, the relatively low temperature applied during the bake treatment does not provide sufficient thermal activation for vanadium precipitation. Ferrous carbides (e.g., ε-carbides) can indeed precipitate during the bake treatment but do not measurably contribute hydrogen trapping, consistent with [43].

Density functional theory calculations by Counts et al. [43] suggested that many substitutional solutes in ferrite trap hydrogen with positive binding energies. The M−H binding energy is roughly correlated with the electronegativity and size of the solute atom (M). The binding energy for solute vanadium was calculated as 0.01 eV (~1 kJ/mol), although it is larger for solute niobium at 0.07 eV (~7 kJ/mol) and titanium at 0.08 eV (~8 kJ/mol). Although these binding energies are rather small in comparison to those of grain boundaries, dislocations, and particle trapping sites, they can still make some contribution to reducing the hydrogen diffusivity in the ferrite matrix. In the present PHS grades, this effect is mostly relevant for vanadium as the solute concentration of niobium and titanium is very low.

5. Conclusions

- Additional microalloying with Nb and V in Ti-based PHS promotes the formation of ultrafine, mixed Ti−Nb−V carbides.
- These particles refine prior austenite grain size, contributing to geometric dilution of hydrogen and improved crack resistance.
- The NbV microalloyed steel tolerates ~0.5 ppmw more diffusible hydrogen than the Ti-only standard variant, a difference attributed to effective hydrogen trapping by nano-sized carbides.
- The hydrogen-trapping potential was validated by estimating particle number density and applying known hydrogen surface coverage values.
- The additional hydrogen tolerance could allow automotive manufacturers to forgo dry-air systems in hot press forming, reducing natural gas use and CO_2 emissions.
- The trapping energy of the nano-sized mixed Ti−Nb−V carbide particles was experimentally measured to be 30.4 kJ/mol (0.31 eV).
- This binding energy is mainly attributed to a chemical interaction between hydrogen and microalloy atoms at the particle–matrix phase boundary in congruence with values reported in the literature.
- Active attraction of hydrogen atoms to the particle interface is not expected since the nano-sized particles after press hardening are incoherent with the martensite matrix.
- It has been assumed that diffusible hydrogen atoms coincidentally approach the incoherent particle boundaries, supported by a small particle average-size as well as a copious distribution with short interparticle distance.

Author Contributions: Conceptualization, F.D. and R.V.; methodology and validation, L.B., H.M. and M.M.T.; formal analysis, R.V.; writing—original draft, R.V.; writing—review and editing, H.M. and R.V.; project administration, F.D. All authors have read and agreed to the published version of the manuscript.

Funding: This research received no external funding.

Data Availability Statement: The original contributions presented in this study are included in the article. Further inquiries can be directed to the corresponding author.

Conflicts of Interest: Author Leonardo Bertini was employed by the company R&D Department, Letomec S.r.l., author Fabio D'Aiuto was employed by the company CBMM Europe BV, author Michele Tedesco was employed by the company Metals Department, Centro Ricerche Fiat S.C.p.A., author Hardy Mohrbacher was employed by the company NiobelCon BV. The remaining author declares that the research was conducted in the absence of any commercial or financial relationships that could be construed as a potential conflict of interest.

References

1. Billur, E. (Ed.) *Hot Stamping of Ultra High-Strength Steels*; Springer International Publishing: Cham, Switzerland, 2019; ISBN 978-3-319-98868-9.
2. Pang, J.C.; Yi, H.L.; Lu, Q.; Enloe, C.M.; Wang, J.F. Effect of TiN-Particles on Fracture of Press-Hardened Steel Sheets and Components. *JOM* **2019**, *71*, 1329–1337. [CrossRef]
3. Hou, Z.; Song, W.; Yi, H.; Wang, J.; Min, J. Fracture Strain of Al–Si-Coated Press-Hardened Steels under Plane-Strain Bending. *Materials* **2022**, *15*, 7345. [CrossRef]
4. Enloe, C.M.; Mohrbacher, H. Influences of Martensite Morphology and Precipitation on Bendability in Press-Hardened Steels. *SAE Int. J. Adv. Curr. Pract. Mobil.* **2022**, *4*, 1181–1188. [CrossRef]
5. Dietsch, P.; Tihay, K.; Bui-Van, A.; Cornette, D. Methodology to Assess Fracture during Crash Simulation: Fracture Strain Criteria and Their Calibration. *Metall. Res. Technol.* **2017**, *114*, 607. [CrossRef]
6. Cai, H.L.; Wang, J.F.; Wu, D.; Yi, H.L. A Simple Methodology to Determine Fracture Strain of Press-Hardened Steels Under Plane Strain Bending. *Metall. Mater. Trans. A* **2021**, *52*, 644–654. [CrossRef]

7. Lai, Q.; Chen, Z.; Wei, Y.; Lu, Q.; Ma, Y.; Wang, J.; Fan, G. Towards the Understanding of Fracture Resistance of an Ultrahigh-Strength Martensitic Press-Hardened Steel. *J. Mater. Res. Technol.* **2023**, *27*, 1996–2006. [CrossRef]
8. Shibata, A.; Gutierrez-Urrutia, I.; Okada, K.; Miyamoto, G.; Madi, Y.; Besson, J.; Tsuzaki, K. Relationship between Mechanical Response and Microscopic Crack Propagation Behavior of Hydrogen-Related Intergranular Fracture in as-Quenched Martensitic Steel. *Mater. Sci. Eng. A* **2022**, *831*, 142288. [CrossRef]
9. Tateyama, Y.; Ohno, T. Atomic-Scale Effects of Hydrogen in Iron toward Hydrogen Embrittlement: Ab-Initio Study. *ISIJ Int.* **2003**, *43*, 573–578. [CrossRef]
10. Nagumo, M. Advances in Physical Metallurgy and Processing of Steels. Function of Hydrogen in Embrittlement of High-Strength Steels. *ISIJ Int.* **2001**, *41*, 590–598. [CrossRef]
11. Birnbaum, H.K.; Sofronis, P. Hydrogen-Enhanced Localized Plasticity—A Mechanism for Hydrogen-Related Fracture. *Mater. Sci. Eng. A* **1994**, *176*, 191–202. [CrossRef]
12. Mohrbacher, H.; Senuma, T. Alloy Optimization for Reducing Delayed Fracture Sensitivity of 2000 MPa Press Hardening Steel. *Metals* **2020**, *10*, 853. [CrossRef]
13. Mohrbacher, H. Property Optimization in As-Quenched Martensitic Steel by Molybdenum and Niobium Alloying. *Metals* **2018**, *8*, 234. [CrossRef]
14. Pressouyre, G.M.; Bernstein, I.M. A Quantitative Analysis of Hydrogen Trapping. *Metall. Trans. A* **1978**, *9*, 1571–1580. [CrossRef]
15. Valentini, R.; De Sanctis, M.; Lovicu, G.; Colombo, C. Helios: A New Method for Hydrogen Permeation Test. 2019. Available online: https://h2tools.org/sites/default/files/ICHS_import/paper_225.pdf (accessed on 13 January 2026).
16. Grabke, H.J.; Gehrmann, F.; Riecke, E. Hydrogen in Microalloyed Steels. *Steel Res.* **2001**, *72*, 225–235. [CrossRef]
17. Chen, Y.-S.; Haley, D.; Gerstl, S.S.A.; London, A.J.; Sweeney, F.; Wepf, R.A.; Rainforth, W.M.; Bagot, P.A.J.; Moody, M.P. Direct Observation of Individual Hydrogen Atoms at Trapping Sites in a Ferritic Steel. *Science (1979)* **2017**, *355*, 1196–1199. [CrossRef]
18. Takahashi, J.; Kawakami, K.; Kobayashi, Y.; Tarui, T. The First Direct Observation of Hydrogen Trapping Sites in TiC Precipitation-Hardening Steel through Atom Probe Tomography. *Scr. Mater.* **2010**, *63*, 261–264. [CrossRef]
19. Ohnuma, M.; Suzuki, J.; Wei, F.-G.; Tsuzaki, K. Direct Observation of Hydrogen Trapped by NbC in Steel Using Small-Angle Neutron Scattering. *Scr. Mater.* **2008**, *58*, 142–145. [CrossRef]
20. Wei, F.-G.; Hara, T.; Tsuzaki, K. Nano-Preciptates Design with Hydrogen Trapping Character in High Strength Steel. In *Advanced Steels*; Springer: Berlin/Heidelberg, Germany, 2011; pp. 87–92.
21. Gui, L.; Zhao, Y.; Feng, Y.; Ma, M.; Lu, H.; Tan, K.; Chiu, P.-H.; Guo, A.; Bian, J.; Yang, J.-R.; et al. Study on the Improving Effect of Nb-V Microalloying on the Hydrogen Induced Delayed Fracture Property of 22MnB5 Press Hardened Steel. *Mater. Des.* **2023**, *227*, 111763. [CrossRef]
22. Cho, L.; Seo, E.J.; Sulistiyo, D.H.; Jo, K.R.; Kim, S.W.; Oh, J.K.; Cho, Y.R.; De Cooman, B.C. Influence of Vanadium on the Hydrogen Embrittlement of Aluminized Ultra-High Strength Press Hardening Steel. *Mater. Sci. Eng. A* **2018**, *735*, 448–455. [CrossRef]
23. Mohrbacher, H. Martensitic Automotive Steel Sheet—Fundamentals and Metallurgical Optimization Strategies. *Adv. Mater. Res.* **2014**, *1063*, 130–142. [CrossRef]
24. Jian, B.; Wang, L.; Mohrbacher, H.; Lu, H.Z.; Wang, W.J. Development of Niobium Alloyed Press Hardening Steel with Improved Properties for Crash Performance. *Adv. Mater. Res.* **2014**, *1063*, 7–20. [CrossRef]
25. Rosenstock, D.; Gerber, T.; Castro Müller, C.; Stille, S.; Banik, J. Process Stability and Application of 1900 MPa Grade Press Hardening Steel with Reduced Hydrogen Susceptibility. *IOP Conf. Ser. Mater. Sci. Eng.* **2022**, *1238*, 012013. [CrossRef]
26. Choo, W.Y.; Lee, J.Y. Thermal Analysis of Trapped Hydrogen in Pure Iron. *Metall. Trans. A* **1982**, *13*, 135–140. [CrossRef]
27. Mohrbacher, H.; Bacchi, L.; Ischia, G.; Gialanella, S.; Tedesco, M.; D'Aiuto, F.; Valentini, R. Characterization of Nanosized Carbide Precipitates in Multiple Microalloyed Press Hardening Steels. *Metals* **2023**, *13*, 894. [CrossRef]
28. Liu, B.; Liao, X.; Tang, Y.; Si, Y.; Feng, Y.; Cao, P.; Dai, Q.; Li, K. Effects of the Addition of Nb and V on the Microstructural Evolution and Hydrogen Embrittlement Resistance of High Strength Martensitic Steels. *Scanning* **2022**, *2022*, 4040800. [CrossRef]
29. *ISO 17081:2014*; Method of Measurement of Hydrogen Permeation and Determination of Hydrogen Uptake and Transport in Metals by an Electrochemical Technique. International Organization for Standardization: Geneva, Switzerland, 2024. Available online: https://www.iso.org/standard/64514.html (accessed on 13 January 2026).
30. Skjellerudsveen, M.; Akselsen, O.M.; Olden, V.; Johnsen, R.; Smirnova, A. Effect of Microstructure and Temperature on Hydrogen Diffusion and Trapping in X70 Grade Pipeline Steel and Its Weldments. 2010. Available online: https://hdl.handle.net/11250/241468 (accessed on 13 January 2026).
31. *ASTM G129-21*; Standard Practice for Slow Strain Rate Testing to Evaluate the Susceptibility of Metallic Materials to Environmentally Assisted Cracking. ASTM International: West Conshohocken, PA, USA, 2021. [CrossRef]
32. *SEP 1970:2011-09*; Test of the Resistance of Advanced High Strength Steels (AHSS) for Automotive Applications Against Production Related Hydrogen Induced Brittle Fracture. Stanford Encyclopedia of Philosophy: Stanford, CA, USA, 2011. Available online: https://www.dinmedia.de/de/technische-regel/sep-1970/149722288 (accessed on 13 January 2026).

33. Georges, C.; Sturel, T.; Drillet, P.; Mataigne, J.-M. Absorption/Desorption of Diffusible Hydrogen in Aluminized Boron Steel. *ISIJ Int.* **2013**, *53*, 1295–1304. [CrossRef]
34. Momotani, Y.; Shibata, A.; Terada, D.; Tsuji, N. Effect of Strain Rate on Hydrogen Embrittlement in Low-Carbon Martensitic Steel. *Int. J. Hydrogen Energy* **2017**, *42*, 3371–3379. [CrossRef]
35. Lin, L.; Li, B.; Zhu, G.; Kang, Y.; Liu, R. Effect of Niobium Precipitation Behavior on Microstructure and Hydrogen Induced Cracking of Press Hardening Steel 22MnB5. *Mater. Sci. Eng. A* **2018**, *721*, 38–46. [CrossRef]
36. Kuhlmann, M.; Schwedler, O.; Holtschke, N.; Jüttner, S. Consideration of Hydrogen Transport in Press-Hardened 22MnB5. *Mater. Test.* **2015**, *57*, 977–984. [CrossRef]
37. Wallaert, E.; Depover, T.; Arafin, M.; Verbeken, K. Thermal Desorption Spectroscopy Evaluation of the Hydrogen-Trapping Capacity of NbC and NbN Precipitates. *Metall. Mater. Trans. A* **2014**, *45*, 2412–2420. [CrossRef]
38. Shi, R.; Ma, Y.; Wang, Z.; Gao, L.; Yang, X.-S.; Qiao, L.; Pang, X. Atomic-Scale Investigation of Deep Hydrogen Trapping in NbC/α-Fe Semi-Coherent Interfaces. *Acta Mater.* **2020**, *200*, 686–698. [CrossRef]
39. Tang, X.; Salehin, R.; Thompson, G.B.; Weinberger, C.R. Long-Range Hydrogen-Binding Effects of Carbide Interfaces in Iron. *Phys. Rev. Mater.* **2021**, *5*, 103603. [CrossRef]
40. Zhang, B.; Su, J.; Wang, M.; Liu, Z.; Yang, Z.; Militzer, M.; Chen, H. Atomistic Insight into Hydrogen Trapping at MC/BCC-Fe Phase Boundaries: The Role of Local Atomic Environment. *Acta Mater.* **2021**, *208*, 116744. [CrossRef]
41. Zhang, S.; Wan, J.; Zhao, Q.; Liu, J.; Huang, F.; Huang, Y.; Li, X. Dual Role of Nanosized NbC Precipitates in Hydrogen Embrittlement Susceptibility of Lath Martensitic Steel. *Corros. Sci.* **2020**, *164*, 108345. [CrossRef]
42. Craig, B.D. On the Elastic Interaction of Hydrogen with Precipitates in Lath Martensite. *Acta Metall.* **1977**, *25*, 1027–1030. [CrossRef]
43. Counts, W.A.; Wolverton, C.; Gibala, R. First-Principles Energetics of Hydrogen Traps in α-Fe: Point Defects. *Acta Mater.* **2010**, *58*, 4730–4741. [CrossRef]

Disclaimer/Publisher's Note: The statements, opinions and data contained in all publications are solely those of the individual author(s) and contributor(s) and not of MDPI and/or the editor(s). MDPI and/or the editor(s) disclaim responsibility for any injury to people or property resulting from any ideas, methods, instructions or products referred to in the content.